ISSN 8755-6839

SCIENCE OF **TSUNAMI HAZARDS**

Journal of Tsunami Society International

Volume 31 **Number 3** **2012**

TSUNAMI PROPAGATION OVER THE NORTH PACIFIC: DISPERSIVE AND NONDISPERSIVE MODELS

Juan Horrillo,
Texas A&M University at Galveston (TAMUG),

William Knight,
NOAA / West Coast & Alaska Tsunami Warning Center, Palmer, Alaska,

Zygmunt Kowalik,
Institute of Marine Science, University of Alaska Fairbanks, Fairbanks, AK. 99775, USA
(zkowalik@alaska.edu).

ABSTRACT

Hydrostatic (HY) and non-hydrostatic (NHY) tsunami physics is compared by application to the Kuril Island Tsunami (KIT) of November 2006 and the Japan Tsunami (JT) of March 2011. Our purpose is to study the significance of dispersive vs. non-dispersive long waves on global tsunami propagation. A tool which is well suited to revealing tsunami wave transformations is the energy flux. Expressions for dispersive and non-dispersive fluxes have been formulated. This provides an understanding of the role of dispersion in tsunami propagation and dissipation. Separating the pressure field into two parts i.e., HY and NHY shows that dispersive waves extract energy from the main wave, directing the dispersive energy flux away from the wave front. The major result of the application of the energy flux to non-dispersive waves is an enhanced understanding of later tsunami wave train arrivals at distant points – with arrivals sometimes occurring several hours after an initial forerunner wave. Computations show that strong differences between non-dispersive and dispersive waves develop along the length of the main energy beam. This has important consequences for accurate tsunami prediction and warnings.

Key Words: *Japan and Kuril tsunamis, hydrostatic and non-hydrostatic numerical modeling, dispersive and non-dispersive energy flux*

Science of Tsunami Hazards, Vol. 31, No. 3, page 154 (2012)

1. INTRODUCTION

Analysis of the data recorded during the Indian Ocean Tsunami of December 2004 demonstrated that the tsunami waves were noticeably dispersive (Kulikov 2005; Horrillo et al., 2006). Dispersion effects played a significant role in the JT event as described by Saito et al., (2011). In coastal regions, the dispersive wave trains interacted with the leading wave runups, drawdowns, and reflections from shelf and land, strongly modifying the leading waves. Sato (1996) investigated the role of dispersive wave trains generated during the 1993 Hokkaido earthquake around the southern part of Okushiri Island. Comparison of field data to numerical results demonstrated that it is the dispersion of the wave front which caused focusing of the wave energy at the narrow region along the lee side of the island, increasing the tsunami wave height. Ortiz et al., (2001) demonstrated that analytical and numerical solutions without dispersion, when compared to dispersive solutions, over-estimate the leading wave heights of medium and large tsunamis.

Tsunami models are usually based on the shallow water approximation which ignores the effects of wave dispersion. The main difficulty is properly accounting for the properties of shorter length scale dispersive waves. During initial propagation, wave separation into spectral components with different frequencies and amplitudes occurs. Thus the leading wave is followed by a train of waves formed in its tail. To follow the dispersion process, numerical models need to resolve these ever-shortening length scales. Due to model limitations however, only the first few waves are usually resolved. As early as 1974, Mader showed that the shallow water long-wave equations often failed to adequately resolve shorter wavelength tsunamis.

Dispersive effects in tsunami calculations are usually introduced through the Boussinesq equation, see Dunbar et al. (1991) or Madsen et al. (1999). Their numerical solutions require small spatial steps and use either implicit schemes to maintain numerical stability (Shigihara 2004) or explicit schemes which display strong numerical dispersion (Yoon et al. 2007). By applying various generating mechanisms (sea bottom uplift, currents generated by horizontal translation of bathymetric features) and the Boussinesq equation to the Indian Ocean Tsunami of 2004, Rivera (2006) demonstrated that their model accounted for most of the observed wave characteristics. Grilli et al. (2007) used the Boussinesq model FUNWAVE to quantify dispersive effects. This approach has been applied to the JT of 2011, with and without dispersion terms (Kirby et al. 2012).

As second order numerical schemes lead to an error term proportional to the third derivative, thus approximating the dispersive term in the Boussinesq equation, Imamura and Shuto (1989) constructed a numerical scheme which used numerical dispersion to mimic physical dispersion. The method proved to be effective in delineating the basic properties of the 1960 Chilean tsunami (Imamura et al. 1990). This scheme was further applied to propagation of tsunamis over slowly varying topography by Yoon et al. (2007), thus introducing the possibility of accounting for the dispersion of distant tsunamis.

This study aims to reproduce dispersive and non-dispersive tsunami wave propagation dynamics of

the KIT of 2006 and the JT of 2011. First we describe the depth integrated, NHY model, which is based on the assumption that the pressure can be split into a sum of hydrostatic and non-hydrostatic components (Stelling and Zijlema, 2003; Walters, 2005). Secondly, results of several numerical experiments are described for the KIT and JT that reveal the difference between transoceanic propagation with and without dispersion. To further differentiate the physics associated with HY and NHY components, the respective energy fluxes are introduced. Finally, to draw some conclusions about the importance of dispersion, observations are compared to model results at several locations.

2. BASIC EQUATIONS

In order to identify the important aspects of tsunami global propagation the equations of motion and continuity are formulated in spherical polar coordinates. Here λ, φ and R are defined as longitude, latitude and distance from the Earth's center. If the origin of the system is located on the ocean surface, it is more suitable to introduce a vertical coordinate $z=R-Ro$. Here Ro is the radius of Earth and is equal 6370km. If in the equations of motion in the spherical system of coordinates (see Gill, 1982) the pressure is set as a sum of a HY part ph, and a NHY part q as suggested by Stelling and Zijlema (2003),

$$p = \rho g(\zeta - z) + q = p_h + q \tag{1}$$

the following set will describe the dispersive wave propagation

$$\frac{\partial u}{\partial t} + \frac{u}{R_\circ \cos\phi}\frac{\partial u}{\partial \lambda} + \frac{v}{R_\circ}\frac{\partial u}{\partial \phi} + w\frac{\partial u}{\partial z} - (2\Omega + \frac{u}{R_\circ \cos\phi})(v\sin\phi - w\cos\phi) = -\frac{g}{R_\circ \cos\phi}\frac{\partial \zeta}{\partial \lambda} - \frac{1}{\rho R_\circ \cos\phi}\frac{\partial q}{\partial \lambda} + A_\lambda \tag{2}$$

$$\frac{\partial v}{\partial t} + \frac{u}{R_\circ \cos\phi}\frac{\partial v}{\partial \lambda} + \frac{v}{R_\circ}\frac{\partial v}{\partial \phi} + w\frac{\partial v}{\partial z} + \frac{wv}{R_\circ} + (2\Omega + \frac{u}{R_\circ \cos\phi})u\sin\phi = -\frac{g}{R_\circ}\frac{\partial \zeta}{\partial \phi} - \frac{1}{\rho R_\circ}\frac{\partial q}{\partial \phi} + A_\phi \tag{3}$$

$$\frac{\partial w}{\partial t} + \frac{u}{R_\circ \cos\phi}\frac{\partial w}{\partial \lambda} + \frac{v}{R_\circ}\frac{\partial w}{\partial \phi} + w\frac{\partial w}{\partial z} - \frac{v^2}{R_\circ} - (2\Omega + \frac{u}{R_\circ \cos\phi})u\cos\phi = -\frac{1}{\rho}\frac{\partial q}{\partial z} + A_z \tag{4}$$

$$\frac{1}{R_\circ \cos\phi}\frac{\partial u}{\partial \lambda} + \frac{1}{R_\circ \cos\phi}\frac{\partial}{\partial \phi}(v\cos\phi) + \frac{\partial w}{\partial z} = 0 \qquad (5)$$

It is interesting to notice that the *acceleration* along the vertical direction (eq. 4) is generated by the nonhydrostatic component of the pressure (q) which is a function of the vertical coordinate. In the above equations, u is the velocity in the λ (E-W) direction, v denotes the velocity in the φ (N-S) direction, w is the velocity in the z direction, p is the pressure, t is the time, g is the Earth's gravity acceleration $g=981\ cms{-}2$ and ρ is the water density. The Coriolis parameter will be taken as $f=2\Omega\sin\varphi$. It is a function of the Earth's angular velocity $\Omega=7.29\times10{-}5\ s{-}1$ and the latitude φ. $A\lambda$, $A\ \varphi$ and Az are components of the viscous force.

To the above set of equations the kinematic boundary conditions which define the vertical velocity w at the free surface ($z=\zeta$ (x,y,t)) and at the bottom are added. The depth in our consideration will be composed of two variables, thus $Hb=H\ x,y\ -\eta\ x,y,t$. Here $H(x,y)$ is the still water depth and η is the bottom deformation. The change in bottom shape may be introduced by bottom uplift or downdrop due to an earthquake or submarine landslide.

The total depth is defined as $D=H+\zeta-\eta$. The vertical velocity at the free surface reads,

$$w_\zeta = w_s = \frac{D\zeta}{Dt} = \frac{\partial \zeta}{\partial t} + \frac{u_s}{R_\circ \cos\phi}\frac{\partial \zeta}{\partial \lambda} + \frac{v_s}{R_\circ}\frac{\partial \zeta}{\partial \phi} \qquad (6)$$

and at the bottom,

$$w_{z=-H_b} = w_b = \frac{D(-H_b)}{Dt} = \frac{\partial \eta}{\partial t} - \frac{u_b}{R_\circ \cos\phi}\frac{\partial H}{\partial \lambda} - \frac{v_b}{R_\circ}\frac{\partial H}{\partial \phi} \qquad (7)$$

Assuming that the dispersive waves are long enough, we can still use the long wave approximation and vertically integrate the above system of equations. The vertically averaged equation of continuity is obtained by integrating eq. (5) from the free surface to the bottom and taking into account eqs. (6) and (7).

$$\frac{\partial \zeta}{\partial t} - \frac{\partial \eta}{\partial t} + \frac{1}{R_\circ \cos\phi}\frac{\partial UD}{\partial \lambda} + \frac{1}{R_\circ \cos\phi}\frac{\partial}{\partial \phi}(DV\cos\phi) = 0 \qquad (8)$$

Equations of motion along the horizontal directions (eqs. 2 and 3) can be averaged as well,

$$\frac{\partial U}{\partial t}+\frac{U}{R_\circ\cos\phi}\frac{\partial U}{\partial\lambda}+\frac{V}{R_\circ}\frac{\partial U}{\partial\phi}-(2\Omega+\frac{U}{R_\circ\cos\phi})V\sin\phi=$$

$$-\frac{g}{R_\circ\cos\phi}\frac{\partial\zeta}{\partial\lambda}-\frac{1}{D\rho R_\circ\cos\phi}\int_{-H_b}^{\zeta}\frac{\partial q}{\partial\lambda}dz-\frac{\tau_\lambda^b}{\rho D} \tag{9}$$

$$\frac{\partial V}{\partial t}+\frac{U}{R_\circ\cos\phi}\frac{\partial V}{\partial\lambda}+\frac{V}{R_\circ}\frac{\partial V}{\partial\phi}+(2\Omega+\frac{U}{R_\circ\cos\phi})U\sin\phi=-\frac{g}{R_\circ}\frac{\partial\zeta}{\partial\phi}-\frac{1}{D\rho R_\circ}\int_{-H_b}^{\zeta}\frac{\partial q}{\partial\phi}dz-\frac{\tau_\phi^b}{\rho D} \tag{10}$$

In the above equations, U is the vertically averaged velocity in the λ (E-W) direction, V denotes the vertically averaged velocity in the φ (N-S) direction. It is important to note that the bottom vertical velocity for a time dependent bottom profile differs from the case of constant bottom profile. In the latter case the expression for the vertical velocity at the bottom simplifies to

$$w_{-H_b}=w_b=-\frac{u_b}{R_\circ\cos\phi}\frac{\partial H}{\partial\lambda}-\frac{v_b}{R_\circ}\frac{\partial H}{\partial\phi} \tag{7a}$$

This expression when introduced into the equation of continuity (eq. 8) yields,

$$\frac{\partial\zeta}{\partial t}+\frac{1}{R_\circ\cos\phi}\frac{\partial}{\partial\lambda}\int_{-H}^{\zeta}udz+\frac{1}{R_\circ\cos\phi}\frac{\partial}{\partial\phi}\int_{-H}^{\zeta}(v\cos\phi)dz=0 \tag{8a}$$

The equation of motion along the vertical direction (eq. 4) will require the strongest simplification so that the vertical integration can be applied. First, it can be written in the following transparent form

$$\frac{\partial w}{\partial t}+w_n=-\frac{1}{\rho}\frac{\partial q}{\partial z}+A_z \tag{4a}$$

We simplify the above equation by assuming the vertical velocity is linear in z (Walters, 2005; Proudman, 1953) and the nonlinear wn and viscous Az terms can be neglected. Integrating along the vertical direction we arrive at

$$D\frac{\partial}{\partial t}[\frac{w_s+w_b}{2}]=-\frac{q_s-q_b}{\rho}$$

$$\frac{\partial}{\partial t}[\frac{w_s+w_b}{2}]=-\frac{q_s-q_b}{\rho D}=\frac{q_b}{\rho D} \tag{11}$$

Due to the linear variation the vertical velocity is taken to be the average of its value at the free surface *ws* and at the sea bottom *w b*. Had the actual nonlinear profile of velocity been retained, the complicated multilayered flow would have been considered.

2. AN APPROACH TO SOLUTION

In order to identify important steps in the construction of a general numerical code we shall simplify problem to the *x-z* crossection. In the vertically integrated equation of motion (eq. 9) the unknown term is related to the NHY pressure (*q*),

$$-\frac{1}{D\rho R_\circ \cos\phi}\int_{-H_b}^{\zeta}\frac{\partial q}{\partial\lambda}dz$$

The expression under integral can be rewritten as

$$\frac{\partial}{\partial\lambda}\int_{-H_b}^{\zeta} q dz = \int_{-H_b}^{\zeta}\frac{\partial q}{\partial\lambda}dz + q_s\frac{\partial\zeta}{\partial\lambda} - q_b\frac{\partial(-H_b)}{\partial\lambda}$$

The integral at the left-hand-side is approximated as

$$\frac{\partial}{\partial\lambda}\int_{-H_b}^{\zeta} q dz \approx \frac{\partial}{\partial\lambda}[0.5D(q_s+q_b)]$$

Since the total pressure vanishes at the free surface, therefore *qs* =0, and we can write,

$$\int_{-H_b}^{\zeta}\frac{\partial q}{\partial\lambda}dz = 0.5\frac{\partial}{\partial\lambda}[Dq_b] - q_b\frac{\partial(H_b)}{\partial\lambda} =$$

$$0.5q_b\frac{\partial}{\partial\lambda}(\zeta+\eta-H) + 0.5D\frac{\partial q_b}{\partial\lambda} \qquad (12)$$

Introducing eq. (12) into eq. (9) results in the following:

$$\frac{\partial U}{\partial t}+\frac{U}{R_\circ\cos\phi}\frac{\partial U}{\partial\lambda} = -\frac{g}{R_\circ\cos\phi}\frac{\partial\zeta}{\partial\lambda}-\frac{1}{D\rho R_\circ\cos\phi}[0.5q_b\frac{\partial}{\partial\lambda}(\zeta+\eta-H)+0.5D\frac{\partial q_b}{\partial\lambda}]-\frac{\tau_\lambda^b}{\rho D} \quad (13)$$

As motion is imparted by both hydrostatic and non-hydrostatic forcing, the equation of motion is split

into two parts. Provisional horizontal velocities are obtained with the hydrostatic pressure alone. The final velocities at the next time step are obtained by advancing the provisional values with *q b*. To achieve numerical solution while stepping in time with the time step *T* we split solution of the above equation into two subsets to be solved on the *T/2* time step as,

$$\frac{1}{2}\frac{\partial U}{\partial t} + \frac{U}{R_\circ \cos\phi}\frac{\partial U}{\partial \lambda} = -\frac{g}{R_\circ \cos\phi}\frac{\partial \zeta}{\partial \lambda} - \frac{\tau_\lambda^b}{\rho D} \qquad (14a)$$

$$\frac{1}{2}\frac{\partial U}{\partial t} = -\frac{1}{D\rho R_\circ \cos\phi}[0.5 q_b \frac{\partial}{\partial \lambda}(\zeta + \eta - H) + 0.5 D \frac{\partial q_b}{\partial \lambda}] \qquad (14b)$$

Or using time stepping index m

$$\frac{1}{2}\frac{(U^{m+1/2} - U^m)}{T/2} + \frac{U}{R_\circ \cos\phi}\frac{\partial U}{\partial \lambda} = -\frac{g}{R_\circ \cos\phi}\frac{\partial \zeta}{\partial \lambda} - \frac{\tau_\lambda^b}{\rho D} \qquad (15a)$$

$$\frac{1}{2}\frac{(U^{m+1} - U^{m+1/2})}{T/2} = -\frac{1}{D\rho R_\circ \cos\phi}[0.5 q_b \frac{\partial}{\partial \lambda}(\zeta + \eta - H) + 0.5 D \frac{\partial q_b}{\partial \lambda}] \qquad (15b)$$

The solution of eq (15a) is usually advanced in time by the two-time-level numerical scheme (Kowalik and Murty, 1993; Imamura, 1996). Eq. (15a) is easily solved based on the old values (at the time step *m*) of the velocity and sea level. The new (provisional) velocity *U(m+ 12)* is introduced into (eq. 15b) to further advance the solution. Unfortunately, the solution of the second equation cannot proceed in time until the new value of *qb* is found. For this purpose we combine the equation of motion along the vertical direction (eq.11), the equation of continuity and (eq. 15b). Consider again equation of continuity (eq.5), which upon vertical integration gives,

$$\frac{1}{R_\circ \cos\phi}\frac{\partial U^{m+1}}{\partial \lambda} + \frac{(w_s^{m+1} - w_b^{m+1})}{D} = 0 \qquad (16)$$

Introducing *Um+1* from eq.(15b) into the above equation, *wsm+1* from eq.(11) and *wbm+1* from eq.(7a) we arrive at equation for the unknown pressure *qb*. The detail of numerical solution for this problem is given in Yamazaki et al.,(2008).

4. MAXIMUM AMPLITUDE

Figure 1 describes the bathymetry of the North Pacific used in our computation (based on work by British Oceanographic Data Centre, 2003). Because numerical results will be compared to sea level data collected by Pacific DART buoys, several of these buoy locations are selected. The tsunami signal will be analyzed in a few points located either in the main energy lobe of the tsunami or in the location with the strong dispersive signal.

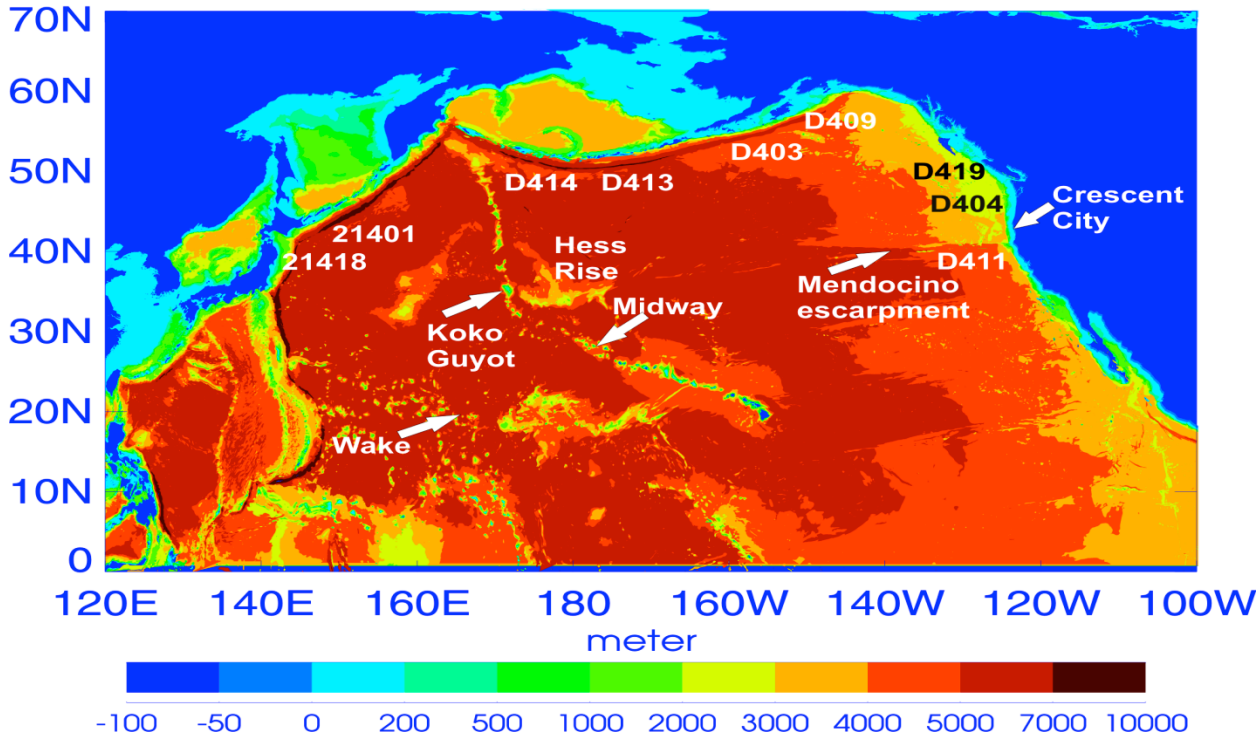

Figure 1. One-minute resolution bathymetry based on the GEBCO Atlas (British Oceanographic Data Centre, 2003). Shown are DART buoys used in comparison with model and some important bathymetric features.

Bathymetric features important in scattering and refocusing tsunami signal are also shown in Figure 1. Primary sources for the tsunami scattering are interactions with Koko Guyot and Hess Rise located at the southern flank of the Emperor Seamount Chain. The regions of the amplified energy flux are usually elongated ridges and fracture zones where tsunami wave energy is concentrated owing to refraction over stepwise topography. An example of such an interaction is the strong tsunami scattering towards Northern California by the Hess Rise and Koko Guyot and later amplified by the Mendocino Escarpment during its approach towards Crescent City (Kowalik et al., 2008). The source for the KIT is described in Kowalik et al. (2008). The JT source is arrived at through the use of Okada's (1985) formulae using fault parameters in Table 1.

Table 1. Fault parameters for Japan earthquake of 11 March 2011.

Fault Parameter	Parameter value
Strike	193°
Dip	19°
Slip	90°
Length	250 km
Width	120 km
Depth	15 km
SW corner Latitude	34.33N
SW corner Longitude	139.33E
Moment	3.0×10^{29}dyne·cm
Rigidity	4.2×10^{11}dyne cm^{-2}

Model computations using the above source were made for 10 hrs of propagation, allowing the tsunami signal to travel over the entire North Pacific. During this computation the maximum tsunami sea surface height (ssh) in every grid point was recorded. The wave height here is defined as positive sea-level change from the mean sea level to the wave crest. The plot of maximum ssh in the North Pacific domain is shown in Fig. 2 for the KIT event and in Fig. 3 for the JT event.

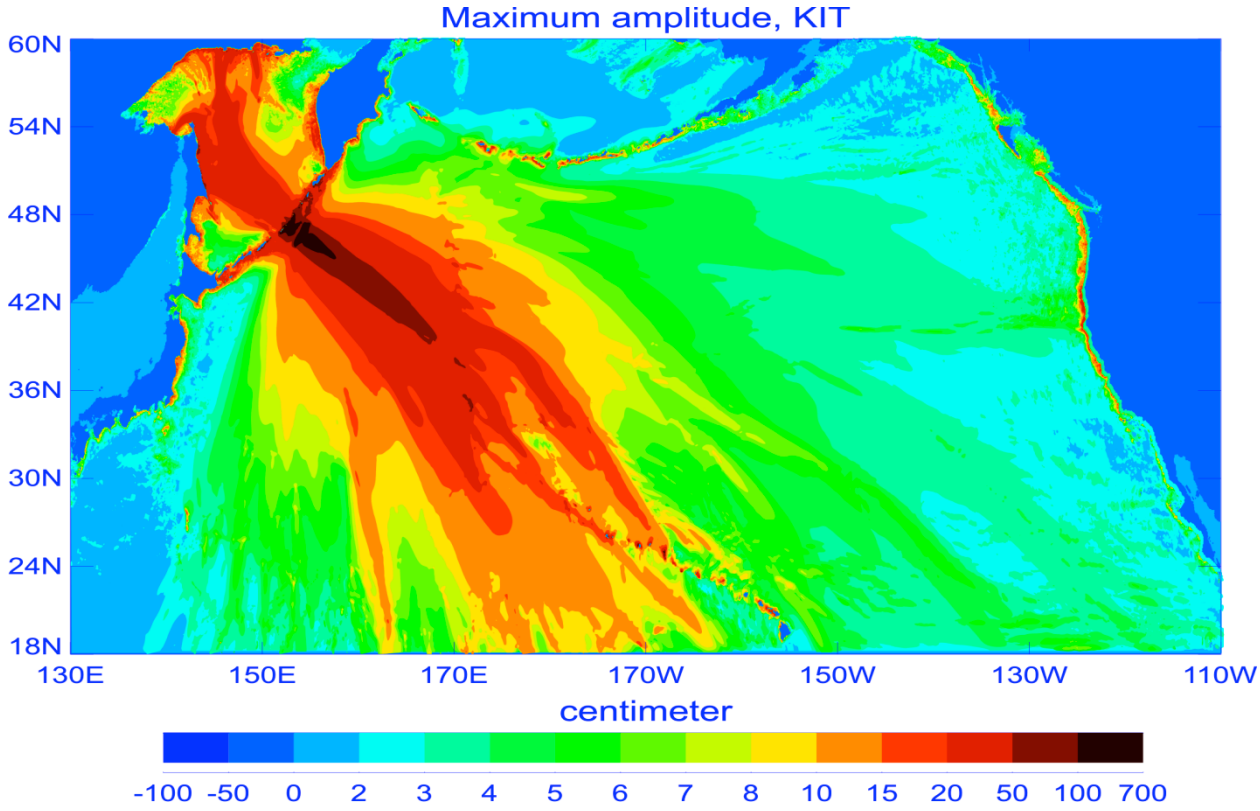

Figure 2. North Pacific, maximum modeled sea surface height, Kurile Island Tsunami, 2006.

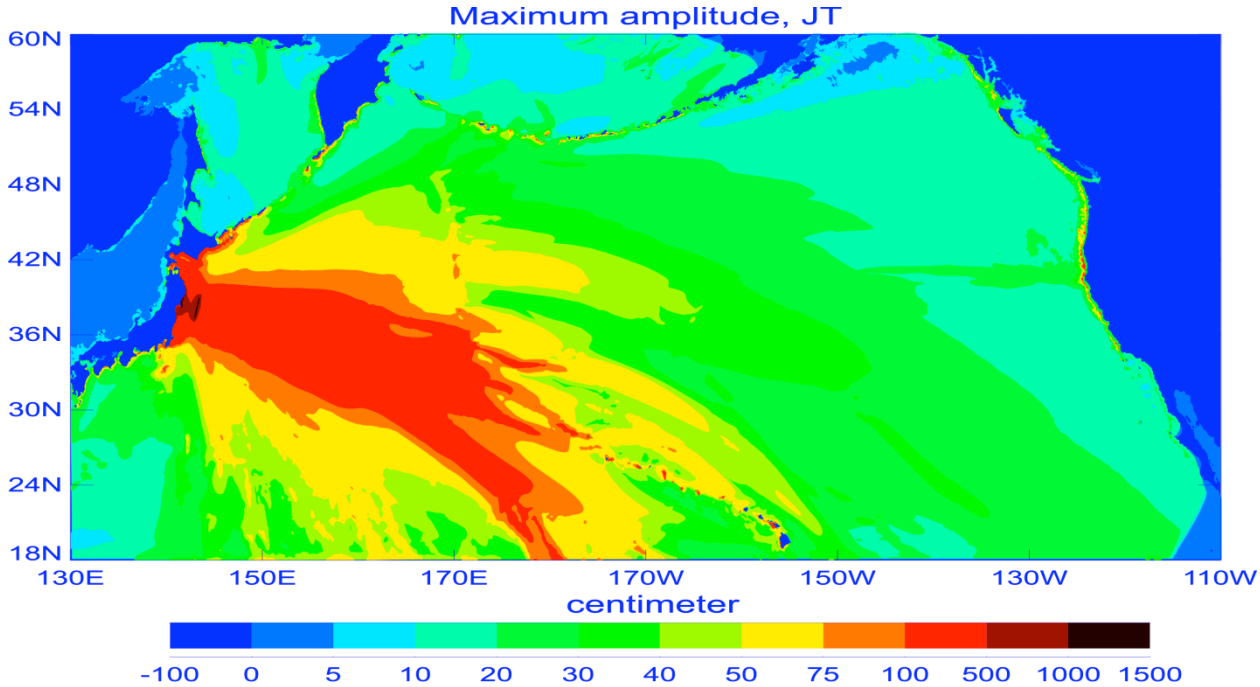

Figure 3. North Pacific, maximum modeled sea surface height, Japan Tsunami 2011.

Computations presented in these figures were carried out using the HY model, therefore NHY pressure q and vertical velocity w are set to zero, and the problem is solved by the set of explicit equations (Kowalik et al., 2005). The signals generated by the source in Kurile Islands Chain and in proximity to Japan are traveling as a positive wave toward the southeast Pacific. Some of the tsunami energy propagates in a finger-like pattern, a product of wave refraction and focusing around islands, seamounts, passages, and chain systems. Closer examination shows that although the signals are dominated by directionality arising from the elongated KIT and JT sources, they also show strong local maxima resulting from interactions with bathymetry. The details of such interactions have been clearly shown by Kowalik et al. (2008). The finger-like patterns of the energy lobes in Figures 2 and 3 can be easily associated with major bathymetric features. The energy lobe resulted from interaction with the Emperor Seamount Chain and especially with two bathymetric features namely Koko Guyot and Hess Rise located at the southern tip of the chain is redirecting energy towards the Crescent City for both KIT and JT events.

The addition of the dispersive wave component to the solution produces a distribution of maximum ssh quite similar to the one from Figures 2 and 3, although the area of the maximum seems to be smaller than that for the non-dispersive propagation. To compare the results for the nondispersive and dispersive wave propagation (notice that we compare only positive ssh) the maximum ssh for the dispersive waves is subtracted from the maximum ssh for the non-dispersive waves. The differences are given in Fig. 4 and Fig. 5. Both figures show a repeatable pattern: in the main energy lobe the hydrostatic solution dominates strongly while at the side lobes, elongated domains dominated by dispersive waves are generated.

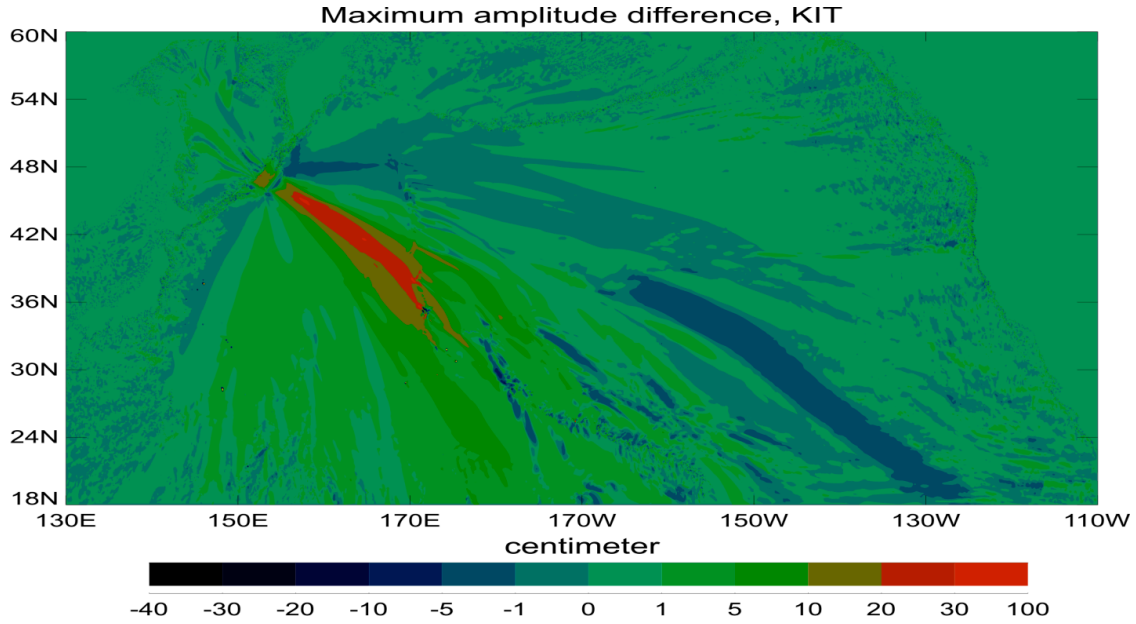

Figure 4. Difference between nondispersive and dispersive maximum ssh, for KIT. Red-green: the nondispersive waves dominate; blue: the dispersive waves dominate.

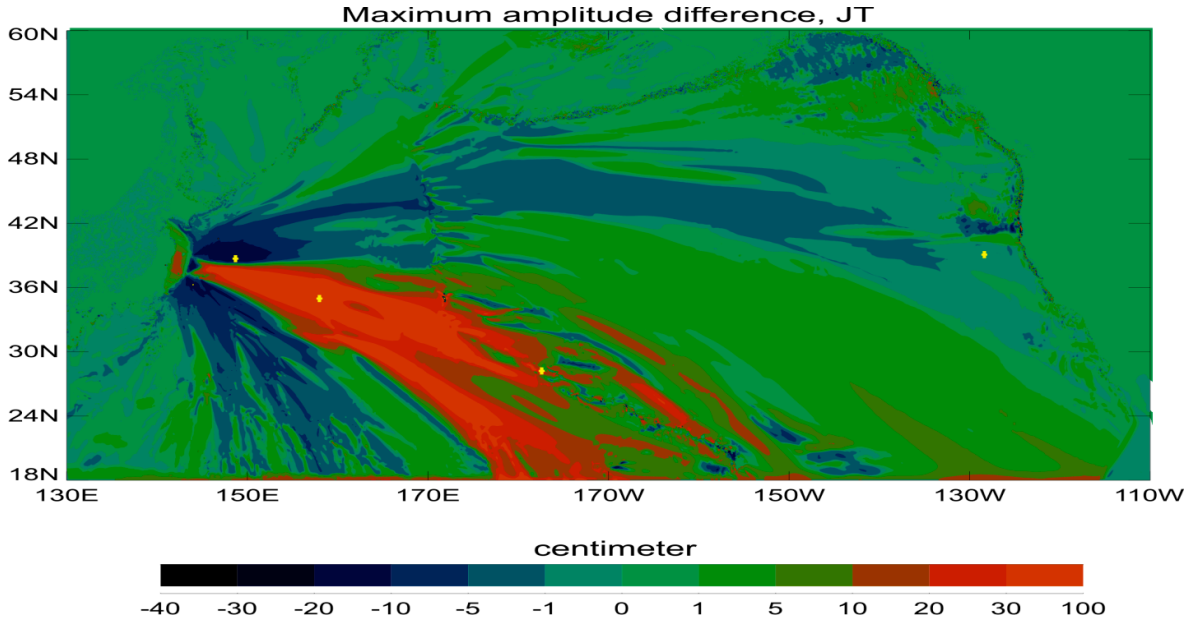

Figure 5. Difference between non-dispersive and dispersive maximum ssh, for JT. Red-green: the nondispersive waves dominate; blue: the dispersive waves dominate. Yellow plus markers indicate: Dart Buoy 21418 (148.694 E,38.711 N), numerical gauge located in main lobe of energy (158.00E, 35.00N), Midway Island tide gauge(177.36 W, 28.212 N) and Dart Buoy 46411 (127 W, 39.94 N).

This pattern confirms previous computations by Kirby et al. (2012) using Boussinesq wave model for propagation of the weakly dispersive surface gravity waves. While comparisons of the dispersive and non-dispersive computations for the same source suggest that the dispersive wave amplitude is typically smaller than the non-dispersive amplitude (Mader, 2004; Horrillo et al, 2006), the above results suggest that over large regions, the opposite situation may occur. The strongest differences for both KIT and JT occur along the main energy lobe where the largest ssh occurs. According to eq. 15b the generation of the dispersive component is connected to the areas where either strong gradients of depth or sea level occur. It points to the regions of the maximum ssh in Figs. 2 and 3 as the area where the strong dispersive effect are generated as depicted in Figs. 4 and 5.

5. ENERGY FLUX

We have used energy fluxes to elucidate the amplification processes during the KIT propagation towards Crescent City (Kowalik et al., 2008). The energy fluxes have been also applied for identification of the sources of the high amplitude secondary signals and to define time delays between initial tsunami wave and secondary signals. Two types of energy fluxes directed in the horizontal plane will be used in the present investigations (see Appendix).

The components of the energy flux vector for the hydrostatic vertically integrated equations

$$\vec{e}_{f,h} = \{UD[\rho(U^2 + V^2)/2 + \rho g\zeta]; DV[\rho(U^2 + V^2)/2 + \rho g\zeta]\} \qquad (17a)$$

and the components of the energy flux generated by the non-hydrostatic pressure q

$$\vec{e}_{f,nh} = \{UDq_b/2; DVq_b/2\} \qquad (17b)$$

We start by plotting distribution of energy flux vectors for the KIT in the North Pacific for the region extending from the Okhotsk Sea to the Emperor Seamount Chain (Fig. 6). The energy flux vectors have the same length but the colors indicate intensity: the red indicates highest, the green is intermediate and the blue is the lowest intensity. The plot captures energy flux vectors at the time of 84 min from the tsunami onset. The upper panel defines the energy flux due to the non-dispersive waves (eq. 17a) and the lower panel identifies the energy flux pattern for the dispersive waves (eq. 17b). The practical application of the energy flux is related to the fact that it delineates the pathways that couple tsunami energy sources with distant location. As can be gleaned from Fig 6 (upper and lower panel) only in one respect are dispersive and non-dispersive energy fluxes similar, namely both energy vector fields at the tsunami wavefront point in the direction of propagation.

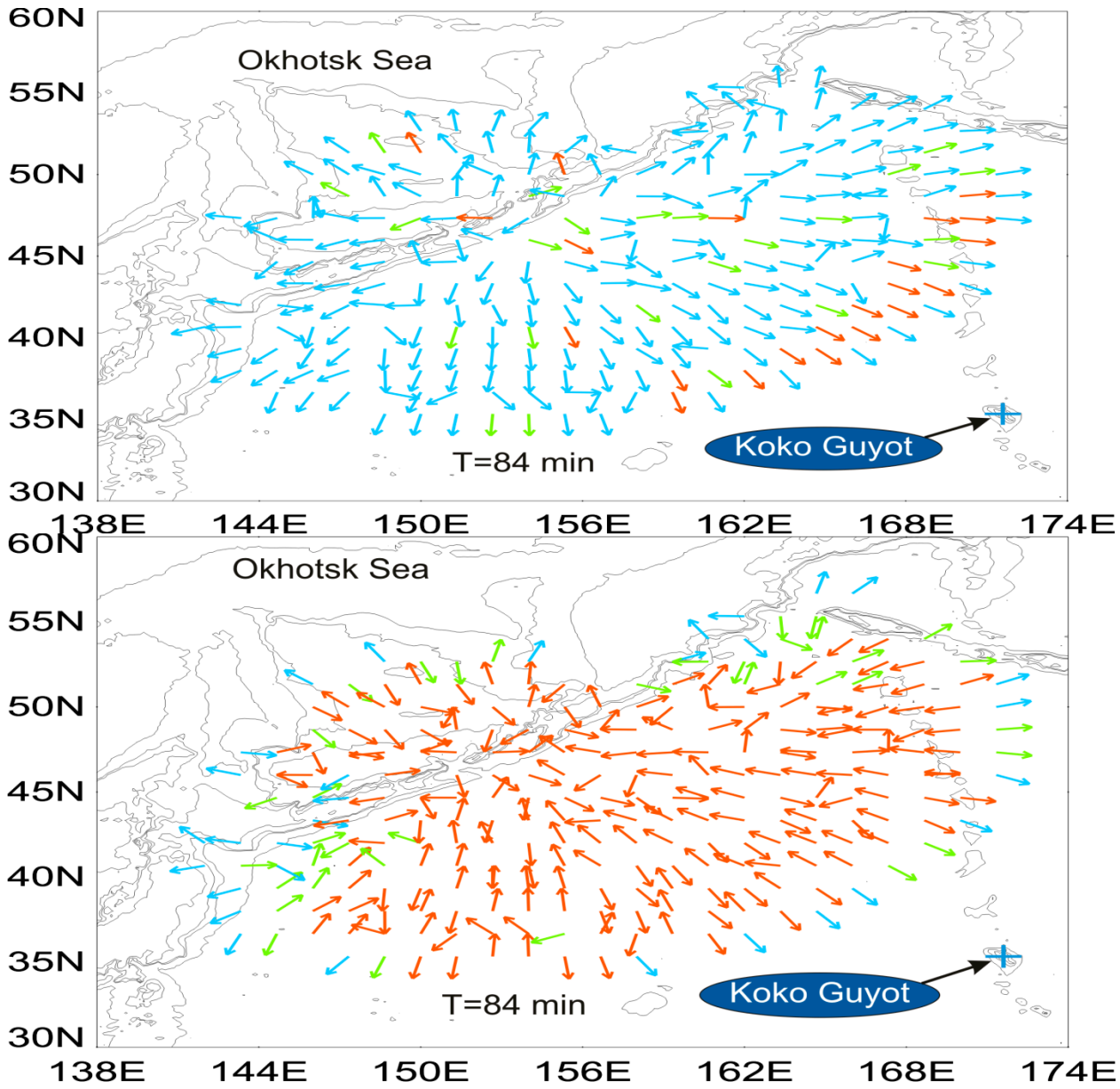

Figure 6. Energy flux vectors over the North-East Pacific at 84 min from KIT onset. Upper panel: nondispersive energy flux; Lower panel dispersive energy flux. Colors define intensity, blue - lowest, green- intermediate, red - highest.

The lower panel of Fig. 6 indicates that as soon as the initial tsunami signal begins to grow at a distant location, dispersive energy is generated and re-directed from the wave front back into the propagation domain. Secondary waves propagating within the domain will receive this additional energy. This "strange" behavior is easily understood if we notice that the non-hydrostatic pressure (q) in the energy

flux eq. 17b is a function of the vertical velocity. According to eq. 11 the pressure (q) is a function of the vertical velocity at the surface and at the bottom.

The generation of surface velocity starts when the tsunami impinges on the new location, increasing the sea level amplitude and causing strong vertical acceleration. Consequently, dispersive waves will be generated and their energy amplified. We can conclude that the largest tsunami wave amplitude (which usually is located just behind the wave front) is the main energy source for the non-dispersive energy flux.

The lower panel in Fig. 6 shows that the energy flux of the dispersive wave is not uniform, although, generally the flow is directed backward towards the Kurile Islands where the tsunami originated. The energy flux vectors depict small-scale variations due to either bottom velocity or to diffraction. A very different pattern of energy flux is displayed for the non-dispersive waves in the upper panel, Figure 6. The energy flux is directed away from the source function (located in the Kurile Islands) with distinctive regions of higher and lower energy fluxes.

As the above analysis identifies the sources of the non-dispersive and dispersive energy fluxes, the next step is to use the fluxes to describe the energy pathways. The source for the non-dispersive waves is well defined in space; on the other hand the source area of the dispersive waves increases at every time step while the intensity of the generation rapidly diminishes.

To further study the KIT and JT development in time the energy flux contours can be used. The contours are given by

$$E_h = \sqrt{e_{f,hx}^2 + e_{f,hy}^2} \quad \text{for eq. 17a} \quad \text{and} \quad E_{nh} = \sqrt{e_{f,nhx}^2 + e_{f,nhy}^2} \quad \text{for the eq. 17b} \quad (18)$$

The energy flux contours for the non-dispersive wave are given in Fig. 7. The well-defined energy flux contours at the front display two closely spaced maxima which are related to the initial wave's positive and negative amplitude. These initial two maxima can be easily tracked (Fig. 7). Moreover when the initial wave impinges on an important bathymetric feature (e.g. Koko Guyot) it goes through complicated processes of tsunami energy scattering and trapping.

To identify the Koko Guyot as an important bathymetric feature, we plot in Fig. 7 the energy flux contours immediately following passage of the main energy lobe past Koko, during KIT (upper panel) and during JT (lower panel).

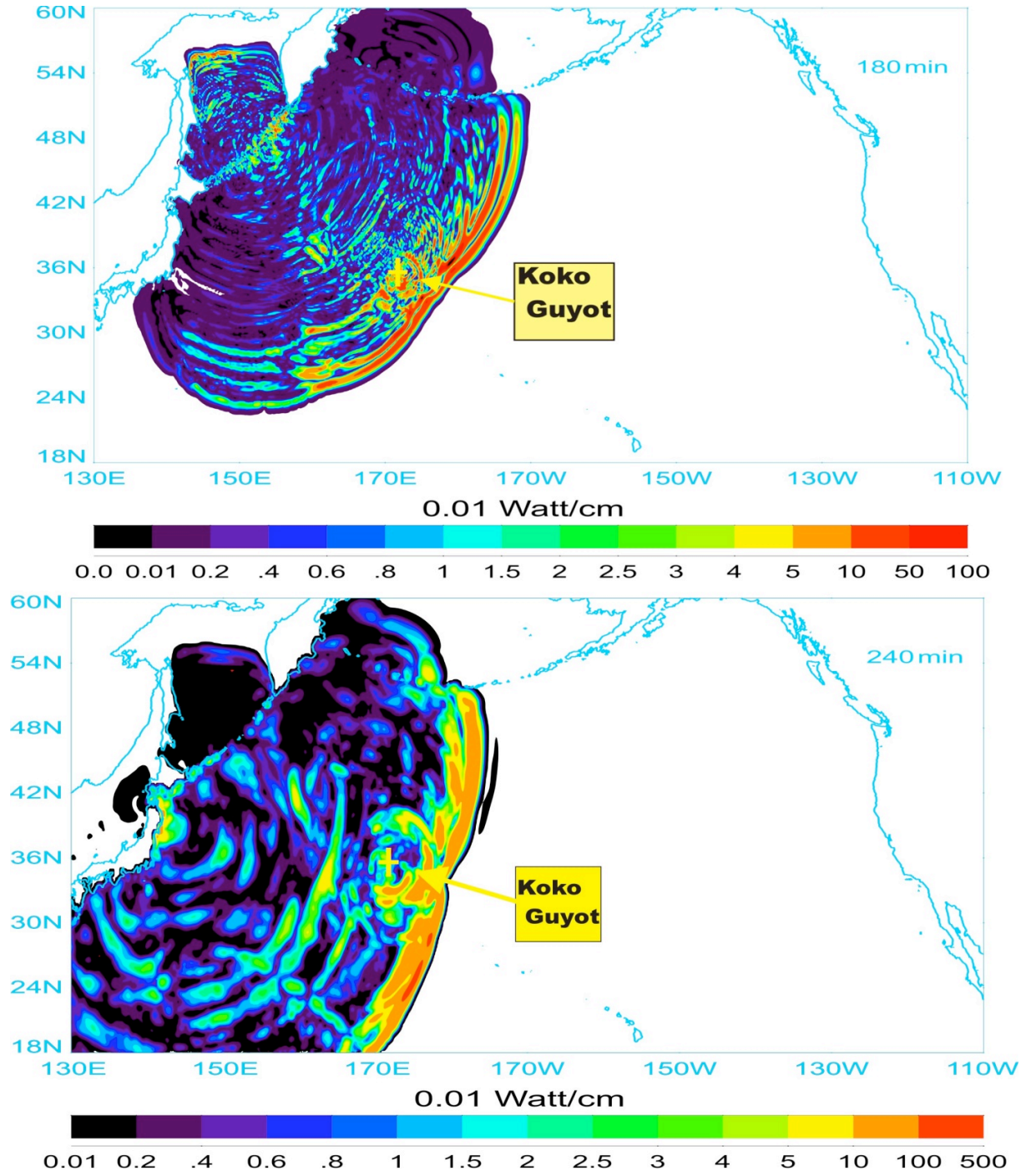

Figure 7. Energy flux contours for the non-dispersive waves, Kurile Island Tsunami (upper panel) and Japan Tsunami (lower panel). The signals of higher energy have been identified as scattered from the Koko Guyot, the Emperor Seamounts and Hess Rise. Yellow plus marker points to location of the Koko Guyot seamount.

Further time history for the KIT as discussed by Kowalik et al. (2008) shows that the wave scattered from the Koko Guyot was responsible for the maximum amplitude at Crescent City which occurred about two hours after the initial wave arrival. Very similar time-history took place during JT. In both events additional tsunami energy enhancement was caused by the Mendocino Escarpment and the local offshore bathymetry (Horrillo at al., 2008).

In conclusion, energy fluxes provide a tool which allows one to not only track the primary sources of energy, but to identify sources of the high amplitude secondary signals and to define the time delay between initial tsunami wave and secondary signals. Computational experiments using energy flux clearly identify the bathymetric features important in scattering tsunami energy towards distant locations. This is possible because the energy flux clearly connects specific bathymetric features such as Koko Guyot and the Hess Rise to impact locations thousands of kilometers away. Although this report is focused on the US West Coast, Koshimura et al. (2008) showed that the KIT energy was similarly scattered westward from the Emperor Seamounts, strongly affecting tsunami energy along Japan's Pacific coast.

6. TIME SERIES

To demonstrate the different behavior of the dispersive and nondispersive wave we consider a few time series of the sea level computed and recorded during JT event. The first point (Fig. 5, yellow cross) denotes location of the Dart Buoy 21418 (148.694E, 38.711N).

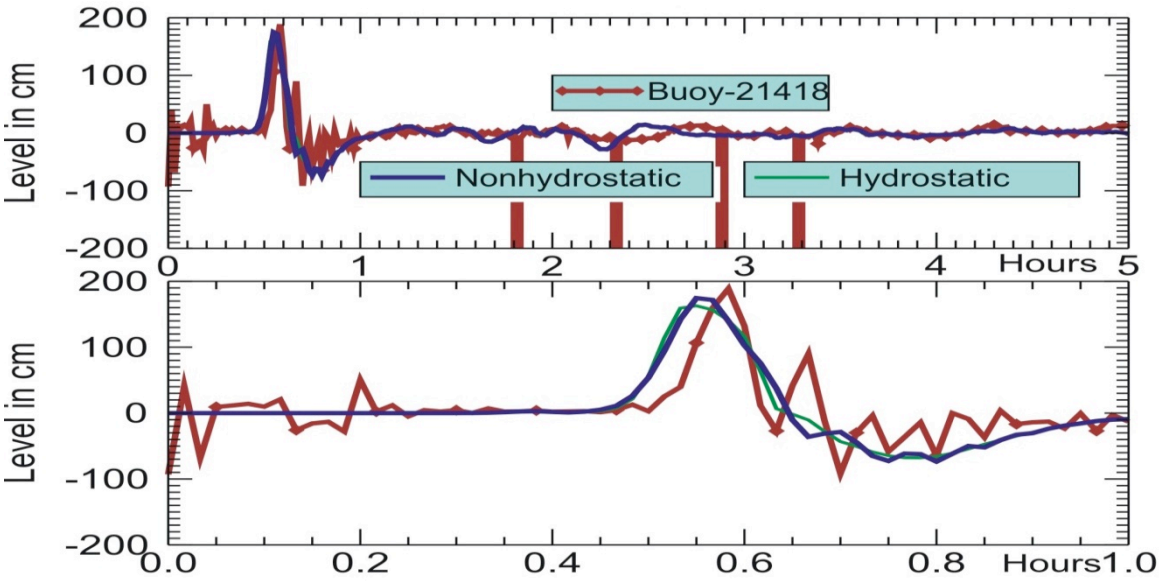

Figure 8. Sea level during Japan Tsunami of 11 March 2011. Red color denotes data recorded by DART buoy; blue denotes the dispersive computation and green non-dispersive. Time is given from the tsunami onset. Lower panel shows detail of the tsunami wave front.

The comparison of the tsunami signal recorded by DART buoys and calculated by the HY and NHY models show that both models reproduced the observed sea level variations. The signal zoom up given in the lower panel of Fig. 8 shows that dispersive wave is dominating and is slightly closer to observations.

The second point chosen for comparison is located in the main lobe of energy (158.00E, 35.00N).

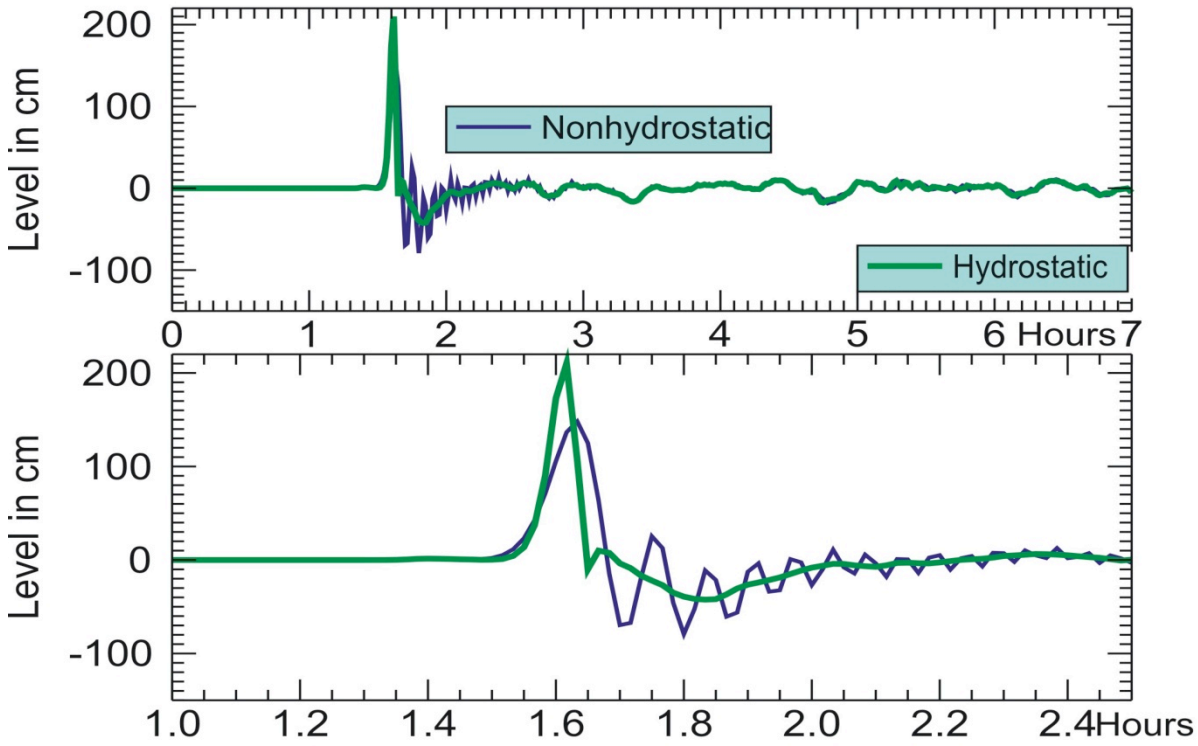

Figure 9. Sea level during the Japan Tsunami of 11 March 2011, calculated inside the main energy lobe (158.0E, 35.0N). Blue line denotes the dispersive computation and green nondispersive. Time is given from the tsunami onset. Lower panel shows detail of the tsunami wave front.

The dispersive versus non-dispersive computations given in Fig. 9 show distinctive features of tsunami wave: A) The amplitude of the first half- cycle for the long wave non-linear, non-dispersive model is much higher than for the dispersive wave (the difference is more than 60 cm); B) The dispersive wave travels slower and C) The train of dispersive waves develops behind the main wave. This train depicts both diminishing amplitude and shorter period. The latter feature, i.e. generation of the short period waves brings into focus the limitations of numerical modeling related to the simulation of short spatial and temporal scales. Simply speaking as the model does not resolve short length scales; the computation develops large numerical errors.

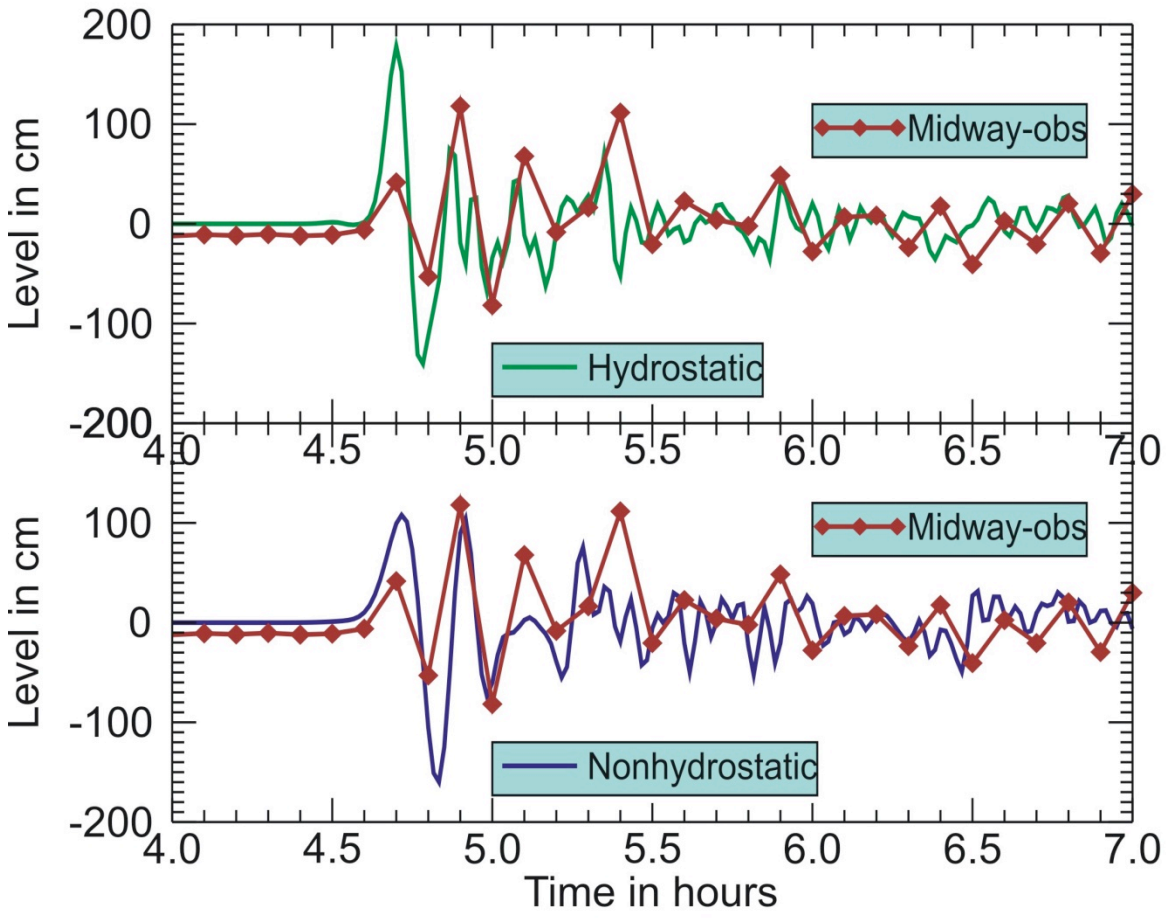

Figure 10. Sea level during Japan Tsunami of 11 March 2011 at Midway Island. Red color shows observation, blue denotes the dispersive and green non-dispersive computations. Time is given from the tsunami onset.

In Fig. 10 the sea level observations made at the Midway Island (177.36 W, 28.212 N) are compared against the nondispersive model (upper panel) and dispersive model (lower panel). Comparison shows that both models reproduce the first recorded waves rather poorly. The dispersive model did the better job when compared with nondispersive model by diminishing the first wave arrival by 70 cm.

Next we consider recording of the sea surface oscillations at the Dart Buoy 46411 (127 W, 39.94 N) located at the far field from tsunami generation function. Comparisons given in Fig. 11 show that both numerical models reproduce well the first waves. The differences between the dispersive and nondispersive models are small. We can conclude that at least for the first waves the dispersion does not change the tsunami wave in this region.

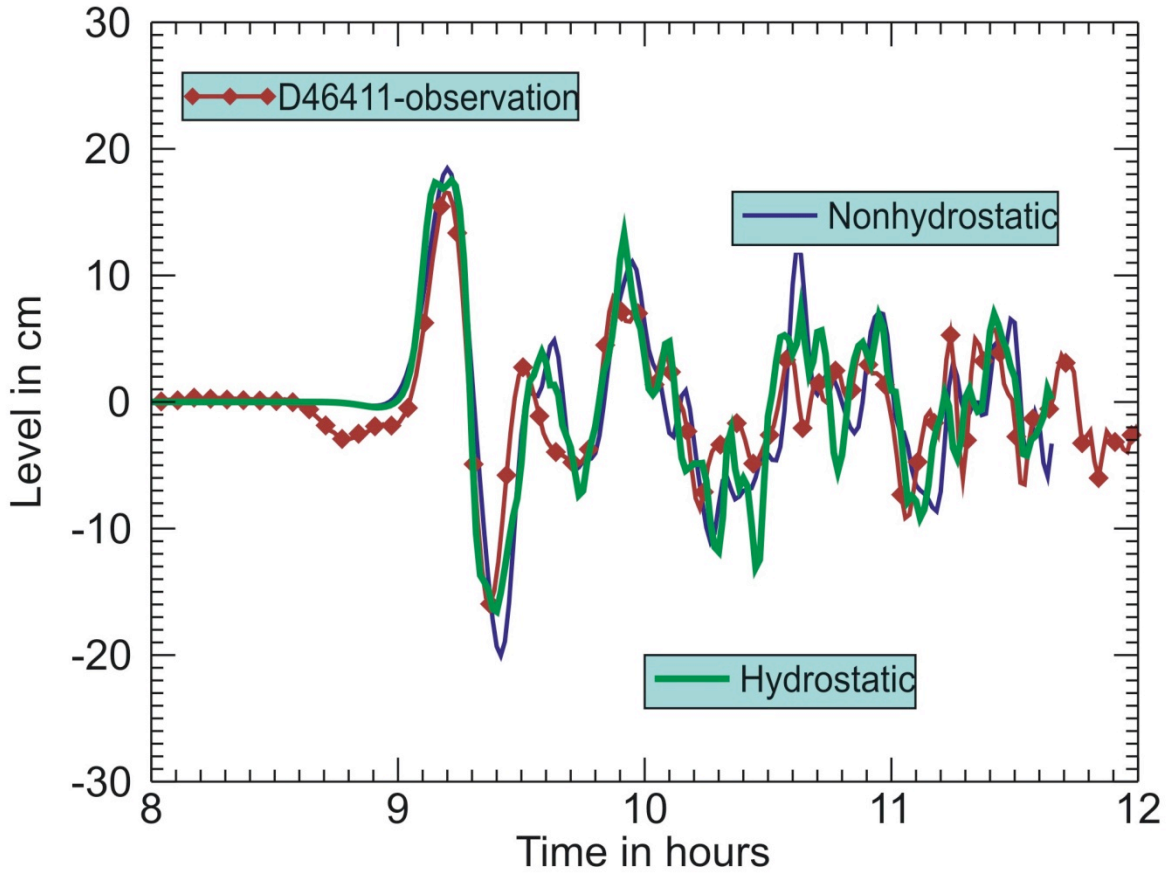

Figure 11. Sea level during Japan Tsunami of 11 March 2011 at the Dart Buoy 46411 (127 W, 39.94 N). Red color shows observation, blue denotes the dispersive and green non-dispersive computations. Time is given from the tsunami onset.

7. DISCUSSIONS AND CONCLUSIONS

The main purpose of the present study was to examine the trans-oceanic tsunami propagation for the KIT and JT where numerical simulation is done with the help of the nonlinear long wave equation and with the weakly dispersive gravity waves.

The results can be summarized as follows: (1) within the main energy lobe there exists a large difference between maximum dispersive and non-dispersive wave amplitudes, (2) in the far-field from the tsunami source the differences are small, (3) the transfer of the tsunami wave energy between the non-dispersive and dispersive modes is well confirmed by the energy flux, (4) temporal series from a few locations confirm the importance of dispersion in the main energy lobe as well. With the NHY

model and its HY counterpart, we are in a position to make careful comparisons between these model solutions. The solutions evolve quite uniformly in the region of the main energy lobe but it proves to be difficult to identify categoric differences between the NHY and HY model solutions and observations at the distances far-away from the main lobe. In summary in the region of the main lobe the 'classical' physics has been observed (Fig. 9), namely the amplitude of the first dispersive wave is smaller than the amplitude of the non-dispersive wave. Unfortunately, the computation depicted the large swath where inverse situation occurs, i.e., dispersive wave dominates over nondispersive waves. What is the source of this energy and why the energy fluxes organized such large and coherent areas the dispersive wave domination is difficult to conclude at the present time.

ACKNOWLEDGMENTS

This publication is the result in part of research sponsored by the Cooperative Institute for Alaska Research with the funds from the National Oceanic and Atmospheric Administration under cooperative agreement NA08OAR4320751 with the University of Alaska.

APPENDIX: ENERGY CONSERVATION

Tsunami transformation during generation, propagation and runup can be assessed through equation of energy and associated fluxes (Tinti and Bortolucci, 2000; Dutykh and Dias, 2008).
To consider energy fluxes for the vertically integrated equations we will start with simplified 2D case expressed by equations (11) and (13)

$$\rho D\frac{\partial}{\partial t}[\frac{w_s+w_b}{2}] = -(q_s-q_b) = q_b \qquad (A.1)$$

$$\rho D\Big(\frac{\partial U}{\partial t}+\frac{U}{R_\circ\cos\phi}\frac{\partial U}{\partial\lambda}\Big) = -\frac{g\rho D}{R_\circ\cos\phi}\frac{\partial\zeta}{\partial\lambda}-\frac{1}{R_\circ\cos\phi}[0.5q_b\frac{\partial}{\partial\lambda}(\zeta+\eta-H)+0.5D\frac{\partial q_b}{\partial\lambda}]-\tau_\lambda^b \qquad (A.2)$$

Denoting *ws 2+ wb 2* as *wa*, multiplying the (A.2) by U and (A.1) by *wa* we arrive at

$$\rho D\frac{\partial}{\partial t}[U^2/2]+\frac{1}{R_\circ\cos\phi}\frac{\partial[DU(\rho U^2/2]}{\partial\lambda} = -\frac{g\rho DU}{R_\circ\cos\phi}\frac{\partial\zeta}{\partial\lambda}$$

$$-U[0.5q_b\frac{1}{R_\circ\cos\phi}\frac{\partial(\zeta-H)}{\partial\lambda}+0.5D\frac{1}{R_\circ\cos\phi}\frac{\partial q_b}{\partial\lambda}-\tau_x^bU \qquad (A.3)$$

$$\rho D\frac{\partial}{\partial t}[\frac{w_a^2}{2}] = -(q_s-q_b)w_a = q_b\frac{(w_s+w_b)}{2} \qquad (A.4)$$

First we change the RHS of the above equation using definition of the surface and bottom vertical velocity

$$q_b\frac{(w_s+w_b)}{2}=0.5q_b(\frac{\partial\zeta}{\partial t}+\frac{U}{R_\circ\cos\phi}\frac{\partial\zeta}{\partial\lambda}-\frac{U}{R_\circ\cos\phi}\frac{\partial H}{\partial\lambda})=$$

$$0.5q_b(-\frac{1}{R_\circ\cos\phi}\frac{\partial DU}{\partial\lambda}+\frac{U}{R_\circ\cos\phi}\frac{\partial\zeta}{\partial\lambda}-\frac{U}{R_\circ\cos\phi}\frac{\partial H}{\partial\lambda})$$

and then adding side by side we arrive at energy equation

$$\rho D\frac{\partial}{\partial t}[U^2/2+w_a^2/2+g\frac{\zeta^2}{2}]+\frac{1}{R_\circ\cos\phi}\frac{\partial[DU(\rho U^2/2+\rho g\zeta+q_b/2)]}{\partial\lambda}=-\tau_x^bU \qquad (A.5)$$

The energy flux component along the N-S (φ) direction can be introduced in the analogous way, thus the energy flux along the E-W direction is

$$Fl_{E-W}=UD[\rho(U^2+V^2)/2+q_b/2+\rho g\zeta] \qquad (A.6a)$$

and along N-S direction

$$Fl_{N-S}=DV[\rho(U^2+V^2)/2+q_b/2+\rho g\zeta] \qquad (A.6b)$$

REFERENCES

Dunbar, D., P.Leblond and T.S.Murty. 1991. Evaluation of tsunami amplitudes for the Pacific Coast of Canada. Prog Oceanog. 26, 115-177.

Dutykh, D. and F. Dias. 2008. Tsunami wave energy. In : J. Locat, D. Perret, D. Turmel, D. Demers et S. Leroueil, (editors).

Proceedings of the 4th Canadian Conference on Geohazards: From Causes to Management. Presse de l'Université Laval, Québec, 594 p.

Gill, A.L. 1982. *Atmosphere--Ocean Dynamics.* Academic Press, Intl. Geophysical Series, Vol.30, 662 pp.

Grilli, S. T., Ioualalen, M., Asavanant, J., Shi, F., Kirby, J. T. and Watts, P., 2007, Source constraints and model simulation of the December 26, 2004 Indian Ocean tsunami, J. Waterway, Port, Coast. and Ocean Eng., 133, 414-428.

Horrillo J., Kowalik Z. and Y Shigihara. 2006. Wave dispersion study in the Indian Ocean Tsunami, Dec 26, 2004, Marine Geodesy, 29: 149-166.

Horrillo, J., Knight W. and Z. Kowalik. 2008. Kuril Island tsunami of November 2006: Part II. Impact at Crecent City by local enhancement, J. Geophys. Res., 113, C01021, doi:10.1029/2007JC004404

Imamura, F. and N. Shuto. 1989. Tsunami propagation simulation by use of numerical dispersion. International Symposium on Computational Fluid Dynamics pp.390-395.

Imamura, F., N. Shuto and C. Goto. 1990. Study on numerical simulation of the transoceanicpropagation of tsunamis. Part 2, Characteristics of tsunami propagation over the Pacific Ocean. Zisin (J, Seismol. Soc. Japan), 43:389-402.

Imamura F. 1996. Review of tsunami simulation with a finite difference method. In *Long-Wave Runup Models*, H.Yeh, P. Liu and C. Synolakis, Eds, World Scientific, 25--42.

Kirby, J. T., F. Shi, J. C. Harris and S. T. Grilli. 2012. Sensitivity analysis of trans-oceanic tsunami propagation to dispersive and Coriolis effects. Ocean Modeling, 42pps. (submitted).

Koshimura, S., Y. Hayashi, K. Munemoto and F. Imamura. 2008. Effect of the Emperor seamounts on trans-oceanic propagation of the 2006 Kuril Island earthquake tsunami. Geophysical Research Letters, vol. 35, L02611, doi:10.1029/2007GL032129.

Kowalik, Z. and Murty, T.S. 1993. *Numerical Modeling of Ocean Dynamics*, World Scientific, 481 pp.

Kowalik Z., W. Knight, T. Logan, and P. Whitmore, 2005. Numerical modeling of the global tsunami: Indonesian Tsunami of 26 December 2004. Science of Tsunami Hazards, Vol. 23, No. 1, 40- 56.

Kowalik, Z., J. Horrillo, W. Knight, and T. Logan. 2008. Kuril Islands tsunami of November 2006: 1. Impact at Crescent City by distant scattering, J. Geophys. Res., 113, C01020, doi:10.1029/2007JC004402.

Kulikov E. 2005. Dispersion of the Sumatra Tsunami Waves in the Indian Ocean detected by satellite altimetry.
http://www.pac.dfompo.gc.ca/science/oceans/tsunamis/documents/195610_0_merged_1107633516.pdf

Mader C. L. 1974. Numerical simulation of tsunamis. J. Phys. Oceanogr., 4, 74--82.

Mader C. L. 2004. Numerical Modeling of Water Waves, CRC Press, 274 pp.

Madsen, P. A., and H. A. Schaffer. 1999. A review of Boussinesq-type equations for surface gravity waves. In *Advances in Coastal and Ocean Engineering*, edited by P. L.-F. Liu, pp. 1-94 Volume 5. World Scientific, Singapore.

Okada, Y. (1985). Surface deformation due to shear and tensile faults in a half-space, Bulletin of the Seismological Society of America, v. 75, 1135-1154.

Ortiz, M., E. Gomez-Reyes, H.S. Velez-Munoz. 2001. A fast preliminary estimation model for transoceanic tsunami propagation. ITS 2000 Proceedings 723-739.

Proudman, J. 1953. *Dynamical Oceanography.* Methuen, J. Willey, London, 409 pp.

Rivera, P. C. 2006. Modeling the Asian tsunami evolution and propagation with a new generation mechanism and non-linear dispersive wave model. Science of Tsunami Hazards, Vol. 25, No. 1, page 18--33.

Saito, T. Y. Ito, D. Inazu, and R. Hino. 2011. Tsunami source of the 2011 Tohoku-Oki earthquake, Japan: Inversion analysis based on dispersive tsunami simulations, J. Geoph. Res., vol. 38, L00G19, doi:10.1029/2011GL049089.

Sato, S. 1996. Numerical simulation of 1993 southwest Kokkaido earthquake tsunami around Okushiri Island, Journal of Waterway, Port, Coastal, and Ocean Engineering, v 122, No. 5, 209--215.

Shigihara, Y. 2004. A study on application of non-linear dispersive wave theory to the numerical simulation of tsunami. PhD dissertation, Department. of Engineering, Tohoku University (in Japanese).

Stelling G.and M. Zijlema. 2003. An accurate and efficient finite-difference algorithm for non-hydrostatic free-surface fow with application to wave propagation. Int. J. Numer. Meth. Fluids, 43:1-–23.

Tinti, S., and Bortolucci, E. 2000. Energy of water waves induced by submarine landslides. Pure appl. Geophys., Vol. 157, pp. 281-318.

Yamazaki, Y., Z. Kowalik, and K. F. Cheung. 2008. Depth-integrated, non-hydrostatic model for wave breaking and runup. International Journal for Numerical Methods in Fluids, DOI: 10.1002/fld.1952.

Yoon, S. B. , Ch. H. Lim , and J. Choi. 2007. Dispersion-correction finite difference model for simulation of transoceanic tsunamis. Terr. Atmos. Ocean. Sci., Vol. 18, No. 1, 31-53.

Walters R.A. 2005. A simple-implicit finite element model for non-hydrostatic (dispersive) surface waves. Int. J. Numer. Meth. Fluids, 49, 721--737.